Preferential corrosion of coherent twin boundaries in pure nickel under cathodic charging

Mengying Liu, Matteo Seita, Ta Duong, Winson C. H. Kuo, and Michael J. Demkowicz

Preferential corrosion of coherent twin boundaries in pure nickel under cathodic charging

Mengying Liu [a*], Matteo Seita [b], Ta Duong [a], Winson C. H. Kuo [c], Michael J. Demkowicz [a]

[a] Department of Materials Science and Engineering, Texas A&M University, College Station, TX 77843-3003, USA

[b] School of Mechanical and Aerospace Engineering, Nanyang Technological University, 50 Nanyang Ave. Singapore 639798

[c] Materials Characterization Facility, Texas A&M University, College Station, TX 77843-3471, USA

Corresponding author: myliu@tamu.edu

Abstract

We describe an investigation of microstructure in pure nickel (Ni) after cathodic charging in aqueous electrolyte. Intergranular corrosion occurs on the sample surface and takes the form of long trenches along coherent twin boundaries (CTBs): sites that have often been considered especially resistant to corrosion. Integrating electron backscatter diffraction and x-ray computed tomography, we show that the trenches are formed by the growth and eventual overlap of isolated conical cavities, which, in turn, are aligned with <110>-type directions within CTB planes. The <110>-type orientation is consistent with cavity initiation at high-energy, symmetric incoherent twin boundary facets within CTB planes. Our observations show that, far from being always corrosion resistant, CTBs are especially susceptible to intergranular corrosion under some conditions.

I. INTRODUCTION

Localized corrosion in metals often occurs preferentially at specific weak sites, such as grain boundaries (GBs) [1], triple junctions [2,3], or other microstructural heterogeneities [4]. Previous

studies have therefore attempted to classify the relative susceptibility of different heterogeneities to localized corrosion [1,5]. It has been proposed that GBs with highly coherent atomic structures, especially Σ3 coherent twin boundaries (CTBs), are particularly resistant to localized corrosion [6,7]. This conclusion has motivated efforts to modify material microstructure to maximize the fraction of CTBs and other coherent GBs to impart intergranular corrosion resistance [8-10]. By contrast, we show that—far from being especially resistant—CTBs in pure Ni are especially susceptible to intergranular corrosion under extreme cathodic polarization.

Investigations of intergranular corrosion frequently make use of surface analysis at the corroded location. After exposure to corrosive conditions, surface morphology is characterized using microscopy or microprobes [9-12]. Additionally, recent investigations have also applied tomographic techniques to characterize sub-surface, corrosion-induced features, such as pits [13-15]. In our study, we integrate electron backscatter diffraction (EBSD) and x-ray computed micro-tomography (micro-CT) to determine the shape and depth of locally corroded regions in Ni. Using these methods, we find that intergranular corrosion takes the form of long trenches composed of overlapping conical cavities aligned with <110>-type directions within CTB planes. This finding suggests that corrosion in fact localizes at symmetric incoherent twin boundary (SITB) facets, which are also preferentially <110>-aligned and have substantially higher energy than the coherent facets in CTBs.

Our investigation challenges the view that CTBs in face-centered cubic (FCC) metals, such as Ni, are corrosion resistant under all conditions. However, it also shows that CTBs are not corroded uniformly, but rather that the high energy facets on these boundaries are the corrosion-susceptible sites. These findings shed new light on the fundamental processes governing the response of GBs exposed to corrosive environments. They also have important consequences for

2

predicting and improving the performance of cathodically-protected components made of Ni-base alloys operating in acidic environments, such as down-hole components in sour wells [16].

II. EXPERIMENTAL

We investigated Nickel PURATRONIC samples (99.9945 wt. % pure), obtained from Alfa Aesar. Two specimens were cut to 10 mm × 10 mm × 1.5 mm using a diamond saw. To increase the grain size, both specimens were annealed in a single run in a tube furnace at 1300 ^{o}C in constant Argon flow (10 sccm) for 3 hours. One specimen (specimen A) was cathodically polarized in a 1N H_2SO_4 aqueous electrolyte for 63 hours at a constant current density of 100mA cm^{-2}. As a result of this treatment, specimen A developed distinct trenches on its surface, as detailed in section III. The other specimen (specimen B) did not have any further treatment after annealing, and was used as reference sample.

Surface impurity concentrations were characterized in sample A with x-ray micro fluorescence spectroscopy (μ-XRF) using the Sub-micron Resolution Spectroscopy beamline (SRX, 5-ID) at the National Synchrotron Light Source II (NSLS-II) at Brookhaven National Laboratory (BNL) [17]. A ~1 μm × 1 μm, 18 keV x-ray beam was raster-scanned to collect XRF spectra as a function of location on the surface. Fitting and analysis was conducted using the PyXRF software [18].

We determined sub-surface sample composition by using a combination of secondary-ion mass spectrometry (SIMS) and Rutherford backscattering spectrometry (RBS). SIMS was conducted using a CAMECA IMS 4f ion microprobe. As this analysis method is destructive, we did not apply it to specimen A, and, instead, characterized specimen B. To obtain precise O

concentrations, we calibrated the SIMS depth profiles to surface O concentrations measured by RBS. We used a ^{4}He analyzing beam with an energy of 3.038MeV [19], current of 2 nA, and total fluence of 1.124×10^{15} ions/cm^2. The cross-section for ^{4}He scattering from O exhibits a nuclear resonance at this beam energy, making our measurement especially sensitive to O content within a ~20nm depth from the sample surface. Backscattered ^{4}He were measured by a silicon detector (ULTRA^{TM} Alpha) placed at an angle of 170.5^o with respect to the incident beam.

Optical images of specimen A were acquired using a Nikon D750 optical camera. Scanning electron microscopy (SEM) was performed using a Philips XL 30 SEM. EBSD analysis was performed using a Tescan FERA-3 SEM with an accelerating voltage of 20 kV and acquisition speed of 39.78 Hz. Grain orientations and grain boundary characters were analyzed using the Aztec software by Oxford Instruments. Following Seita *et al.* [20], we identified CTBs as Σ3 boundaries with low curvature surface traces.

High resolution CT scans were obtained using a Phoenix v|tome|x M (by GE Measurement & Control) at the University of Florida. Scanning was carried out using a 180 kV X-ray transmission tube employing a tungsten-on-diamond target, with the following settings: 160 kV, 50 mA current, 500 millisecond detector timing, and a 0.5 mm copper filter. The scan acquired 2500 projections (averaging of five images per rotation position with one skip) with pixel/voxel resolution of 7.7248 μm. The resulting 2D x-ray data were processed by GE's proprietary datos|x software v 2.3.2 using the standard algorithm and a beam hardening correction of 9.3 to produce a 3D data set. The data set was exported as a set of tiff images for analysis in MATLAB. From these images, we reconstructed a 3-D virtual specimen using a specially developed MATALB script. Standard MATLAB routines then enabled us to render the surfaces of these samples as well as view planar cross-sections at any location and plane orientation.

III. RESULTS

A. Impurity content

We conducted a series of tests to determine whether annealing or electrochemical exposure introduced impurities into the specimens. Surface characterization *via* XRF revealed that isolated particles adhering to the surface contained a variety of elements besides Ni, including Fe, Cr, Ca, Cl, and Ti. However, all of these impurities were localized within discrete surface contaminants and none of them appeared to have been incorporated into the sample itself. In particular, there was no evidence of surface impurities within depressions formed by localized corrosion.

Depth profiles obtained by SIMS indicate elevated oxygen (O) impurity content in a surface layer approximately 1μm thick, as shown in FIG. 1.a). To convert these profiles to absolute O concentrations, we calibrated the SIMS data using RBS surface composition measurements, the outcome of which is shown in FIG. 1.b). Surface O atoms are expected to produce a peak at an energy of 1.1 MeV. However, no such peak was observed after five minutes of measurement time. The broad profile seen in FIG. 1.b) is entirely due to ^{4}He backscattering from Ni. Concluding that any surface O peak must therefore be smaller than the standard deviation in the count of ^{4}He backscattered from Ni, we determine that the detection limit of O impurities within a 20 nm surface layer is 3.84 at.%. Rescaling the SIMS data in FIG. 1.a) to this O content within 20 nm of the surface, we find that the O impurity concentration in our sample below a depth of 2 μm is no greater than 0.027 at.%, consistent with data provided by the supplier. These findings are also consistent with the work of Perusin *et al.* [21], who also used SIMS to investigate oxygen content in pure Ni annealed at high temperature.
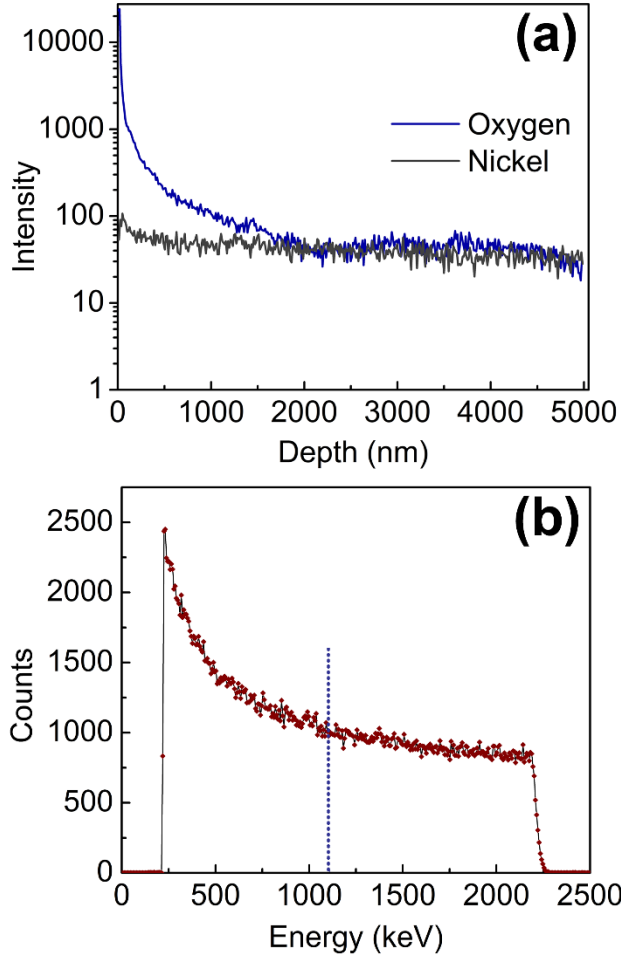
FIG. 1. (a) Unscaled Ni and O depth profiles obtained by SIMS. (b) [4]He backscattering spectrum obtained by RBS. The dotted vertical line indicates the expected energy of a surface O peak.

It is plausible that any O in the 20 nm surface layer, which we characterized by RBS, is actually concentrated into a ~1 nm thick NiO film on the sample surface, as reported by other researchers [22]. However, our measurement does not have sufficient depth resolution to distinguish such a film from a 20 nm-thick solid solution. In light of the XRF, SIMS, and RBS measurements described above, we do not believe that impurities—either on the surface or deep within the sample—are responsible for the surface corrosion features observed on specimen A.

B. Surface imaging

FIG 2.a) shows an optical image of one side of specimen A. The specimen has a smooth, bright surface with occasional long, linear trenches on it, easily visible to the naked eye. The trenches range in length from 0.5 mm to 4 mm. FIG. 2.b) shows an SEM micrograph of one of these trenches. The trench is 100-150 µm wide and appears to be composed of a series of overlapping depressions.
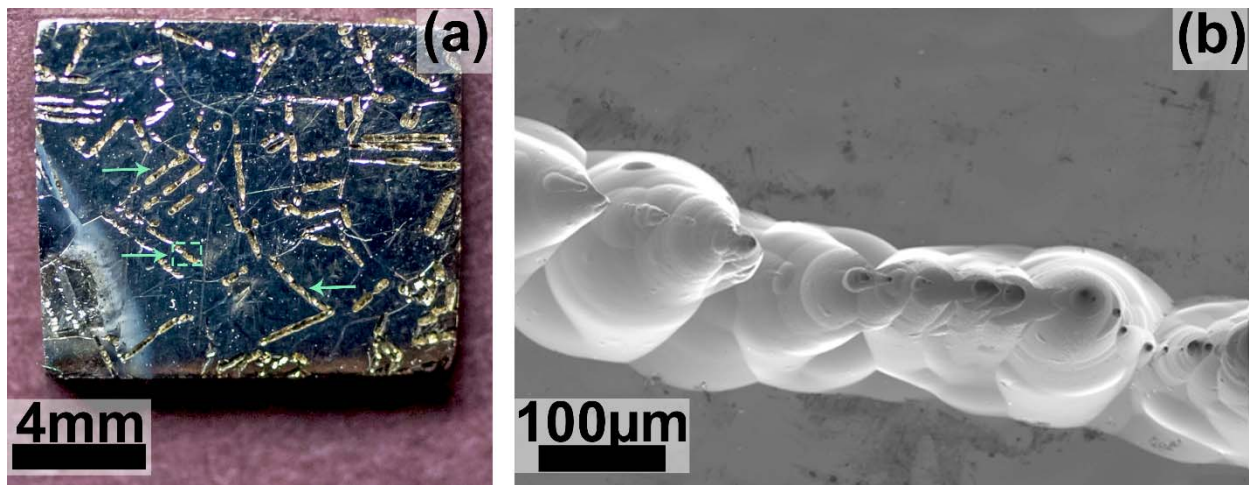

FIG. 2. Optical and SEM images of specimen A. (a) Optical image of specimen A top surface; green horizontal arrows indicate some examples of trenches. (b) SEM image of the trench in the green dashed box in (a).

We performed EBSD measurements to correlate the locations of the trenches in FIG. 2.a) to the microstructure of the specimen. FIG. 3 shows an example of a grain orientation map acquired by this method, with trenches appearing as thick, black lines. Isolated black speckles are due to surface contamination. Our analysis reveals that all of the trenches lie along GBs. Moreover, out

of a total of 91 trenches, 88 lie specifically along Σ3 CTBs. Conversely, nearly all of the CTBs on the sample surface—88 out of a total of 101—have trenches on them. Considering that there are 152 GB traces on the sample surface altogether, our analysis shows that the CTBs in our sample are especially susceptible to localized corrosion under cathodic polarization.
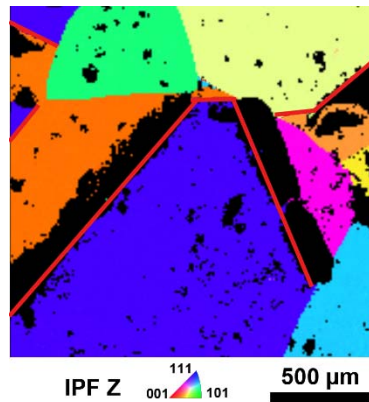

FIG. 3. EBSD image of part of the surface of specimen A (site 3 as indicated in FIG. 4 (b)) with grains colored by crystallographic orientation. Thick, black lines indicate trenches. Σ3 CTBs are marked with red lines. Isolated black speckles are due to surface contamination.

Previous investigations on pure Ni [21] as well as Ni-base alloys [23,24] heat treated in oxygen-bearing atmospheres revealed preferential intergranular oxidation in the form of continuous intergranular metal-oxide films as well as discrete metal-oxide inclusions decorating GBs. The films and inclusions observed in these previous studies were several microns thick, making them easy to discern on sample surfaces and cross sections using SEM. We inspected the surfaces of our samples using high resolution SEM, but did not observe any evidence of such oxide films or inclusions. Moreover, after completing all of our sample characterization, we sectioned specimen

8

A. Examination of the cross-section surface did not reveal any intergranular oxide particles, films, or voids. These findings further reinforce our conclusion that the intergranular corrosion on the surface of specimen A does not originate from the uptake of impurities, such as oxygen, during annealing or electrochemical charging.

C. Trench morphology

The micrograph in FIG. 2.b) suggests that the trenches on specimen A have complex internal morphologies consisting of multiple overlapping cavities. We used x-ray CT to characterize trench morphology in 3-D. FIG. 4 shows a surface rendering of our CT sample reconstruction. In their work on pure Ni annealed at high temperature, Perusin *et al.* [21] observed sub-surface, intergranular voids several microns in diameter. Such voids would have been easily resolvable by CT. However, no such voids were found in the CT reconstruction of our sample. Comparison of FIG. 4. with FIG. 2.a) indicates that the CT scan reproduces the same surface corrosion features as those revealed by optical imaging. The sites demarcated in FIG. 4.b) were selected for closer inspection. These sites were selected for detailed investigation because they contain the most well-defined, unambiguously characterizeable cavities. Moreover, these trenches possess morphologies representative of those typically encountered throughout the entire sample.
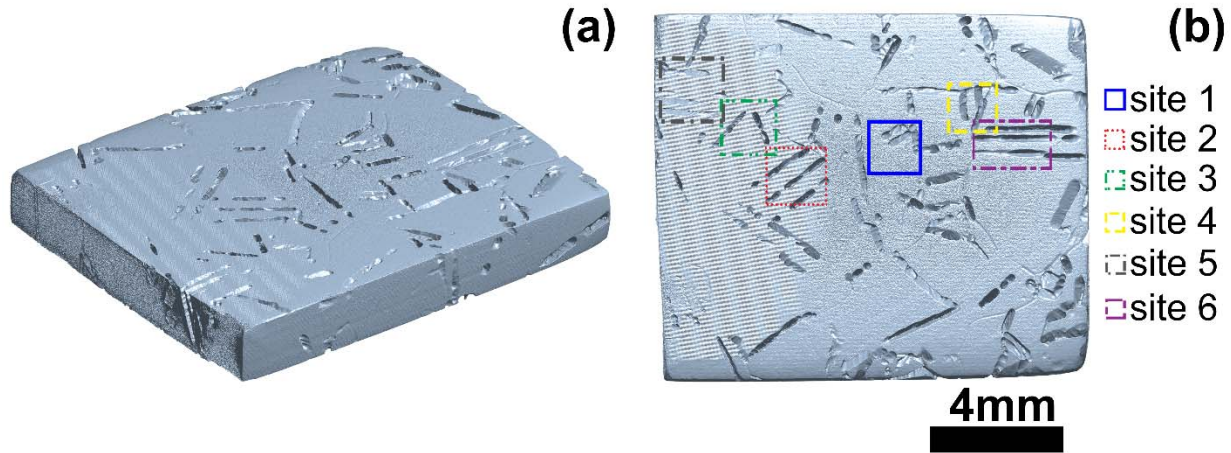
FIG. 4. CT reconstructions of corroded Ni (a) 3-D, (b) 2-D top surface profile. The indicated sites were selected for closer inspection.

FIG. 5 shows perspective views of selected trenches to reveal their morphology. To better expose the shapes of the trench bottoms, the viewing direction is from the sample interior, looking from beneath the trenches up toward the sample surface. FIG. 5 also provides EBSD images of the surface regions near the trenches along with indices correlating the images to sites on specimen A, shown in FIG. 4.b). FIG. 6 shows a more detailed rendering of the trench marked with a green dashed box in FIG. 5.f). Consistent with our deduction from FIG. 2.b), we find that the trench bottoms consist of multiple, discrete cavities. These cavities are approximately conical in shape, with the cone tips pointing into the interior of the specimen and the cone bases emerging onto the surface. The maximum diameters of the cavities are typically about 100 μm and their depths range from 300 to 600 μm. The centerlines of the cavities do not appear to be oriented perpendicular to the sample surface. On the contrary, most of them are distinctly oblique with respect to the surface. Finally, the cavities are not perfectly conical, but rather exhibit curvature along their centerlines and corrugation of their surfaces.

IPF Z (a)

500 μm

IPF Z (b)

500 μm

IPF Z (c)

500 μm

IPF Z (d)

500 μm

IPF Z (e)
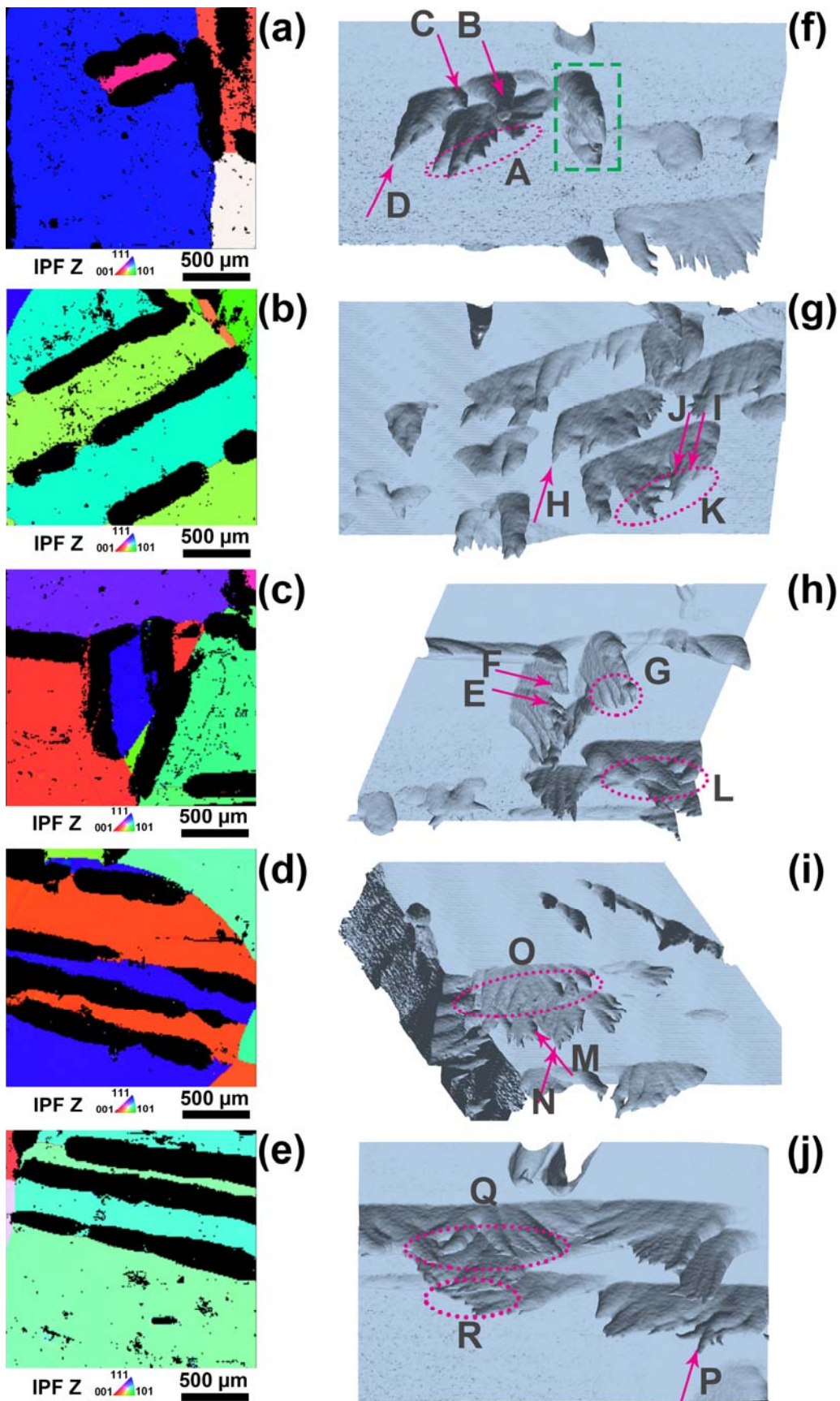
500 μm

(f)

(g)

(h)

(i)

(j)

11

FIG. 5. EBSD images of the sites shown in FIG. 4.b): (a) 1, (b) 2, (c) 4, (d) 5, and (e) 6. Surface

renderings of corresponding trenches with the viewing direction from beneath the trenches

looking up toward the sample surface: (f) site 1, (g) site 2, (h) site 4, (i) site 5, and (j) site 6
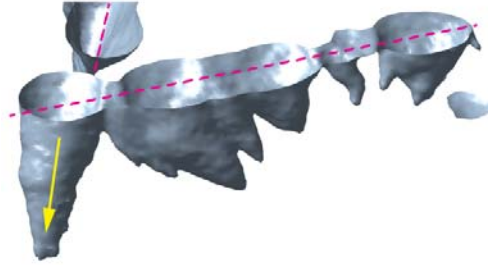

FIG. 6. Rendering of the morphology of the trench identified with a green dashed box in FIG.

5(f). For clarify, the exterior sample surface is not shown. The dashed lines trace cavity

intersections with the free surface. The arrow indicates the direction of the sample interior.

Many of the cavities overlap in the near-surface regions, giving rise to the appearance of long,

linear surface trenches, consistent with FIG. 2.a). FIG. 5 shows several distinct cavity

arrangements along the length of these trenches. The most common arrangement is the "fin"

configuration, e.g. those marked A, G, and R in FIG. 5.f), 5.h) and 5.j), where all cavities have

centerlines oriented in approximately the same direction. This configuration constitutes a clear

indication that the cavities have a preferential growth plane and direction.

Another cavity configuration is the "palm leaf", e.g. Q in FIG. 5.j), where multiple cavities

originate from the same area on the surface but have centerlines pointing in different directions.

Yet another is the "arrow head," e.g. K and L in FIG 5.g) and 5.h), where cavities originate from

different locations on the surface yet have centerlines that intersect beneath the surface. Such configurations form sub-surface channels. A particularly interesting example is O in FIG. 5.i), where cavities emanating from two perpendicular surfaces (the sample top surface and one of the edges) intersect within the interior of the sample, forming a continuous channel between the two surfaces.

D. Crystallography of conical cavities

To analyze the crystallography of the conical cavities, we correlated their positions and morphologies, as characterized by micro-CT, with grain boundary orientations and crystallographic characters obtained from EBSD. To that end, we translated and rotated the micro-CT reconstruction such that it is in registry with the EBSD. Because we kept the sample direction and acquisition coordinate systems fixed when acquiring the EBSD data, this registration procedure only had to be carried out once. During the registration, the CT reconstruction was first translated such that the tip of a pre-selected surface trench in the CT coincided with the tip of the same trench, as obtained by EBSD. Next, the CT reconstruction was rotated such that the sample edges in the CT coincided with the sample edges from EBSD. At the end of this procedure, all features in both the CT reconstruction and EBSD images could be referred to the common Cartesian coordinate system shown in FIG. 7. The registration process was carried out numerically by performing rigid body coordinate transformations on the CT data using MATLAB.
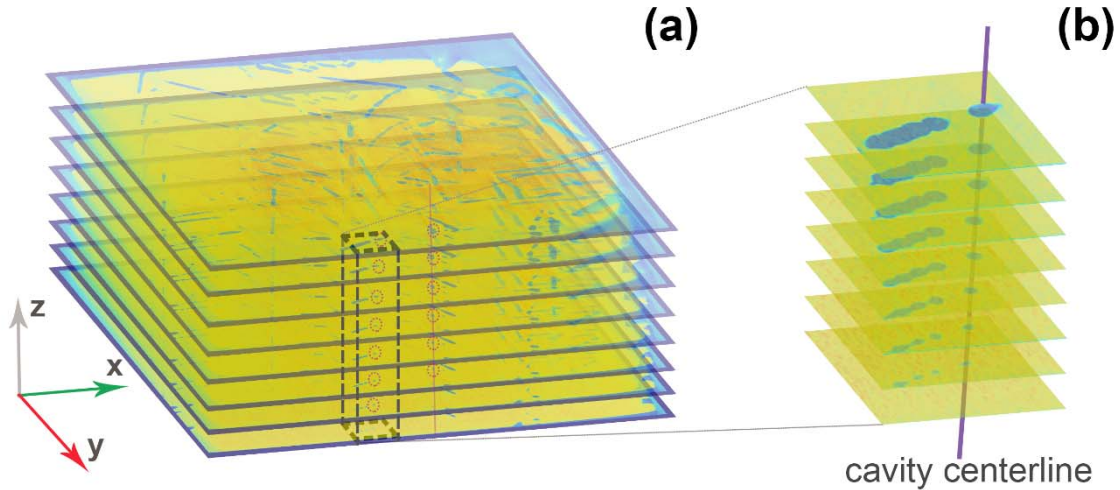
FIG. 7. (a) A series of cross-sections parallel to the surface of the 3-D CT reconstruction obtained at different depths from the surface. Cavity intersections with each slice are marked with red circles. Dashed red lines indicate the cavity centerlines. (b) Magnified view of the black cube in FIG. 7 (a) illustrating the process for determining cavity centerlines.

Next, we acquired virtual cross sections through the CT reconstruction parallel to the surface (x-y) plane at different depths beneath the surface. The intersection of a conical cavity with a cross section plane is an oval. We determined the center point coordinates of these ovals on each cross section. By performing a linear least-squares fit to these coordinates as a function of depth, we determine the orientations of cavity centerlines in the common coordinate system, as shown in FIG. 7. Most fits use 10-12 sets of coordinates at varying depths, though some use as few as 4.

To confirm that a conical cavity lies within a CTB plane, we take the dot product of the cavity centerline direction with the unit vector normal to the CTB plane. The latter may be determined from the crystallographic orientations of the grains adjacent to the CTB, obtained *via* EBSD. Following Seita *et al.* [20], we seek a pair of {111}-type directions in the adjacent grains that are

nearly parallel. Every Σ3 GB has just one such pair. If the CTB plane normal is perpendicular to the cavity centerline direction, then their dot product is zero and the cavity lies within the CTB plane. For any non-zero value of the dot product, we compute an angular deviation of the cavity centerline from the CTB plane. TABLE I reports these deviations for 11 selected cavities, confirming that all of the cavities are well aligned with the CTB planes, to within the measurement uncertainty.

TABLE I. Quantification of cavity centerlines relative to the CTB {111} planes on which they reside and <110>-type directions within these planes. Site labels correspond to those shown in FIG. 5.

Site	B	C	D	E	F	H	I	J	M	N	P
Deviation angle between cavity centerline and CTB plane	1.1±4.4°	0.8±6.7°	2.2±6.9°	0.11±2.2°	0.44±2.6°	0.14±12.4°	0.25±6.0°	0.44±7.6°	0.36±2.9°	1.68±4.0°	0.37±1.7°
Angle between cavity centerline and closest <110> type direction	N/A	5.0±6.8°	4.6±4.6°	8.3±5.0°	4.3±3.4°	21.8±17.0°	3.9±5.4°	2.0±8.2°	13.1±5.6°	3.0±5.8°	10.8±6.8°
Shape classification	variable centerline direction	palm leaf		fin		N/A	fin		arrow head		N/A

Finally, as the cavities lie within the CTB plane, we can investigate the orientation of cavity centerlines with respect to the <110>-type directions present within each CTB plane. For every CTB plane, there are three pairs of <110>-type directions within the adjacent grains that are parallel to each other. We identify these three pairs from the EBSD data, confirm that each has a direction perpendicular to the CTB plane normal, and compare them to the cavity centerlines. We find that most cavities are well-aligned with a <110>-type direction within the CTB plane.

TABLE I reports angular deviations of 11 example cavities from the closest <110>-type direction.

To estimate the uncertainty of the deviation angles reported in TABLE I, we first use the least squares method to find the best fit linear functions, $x = a_0 + a_1 z$ and $y = b_0 + b_1 z$, relating the x and y coordinates of centerline intersections with cutting planes at fixed depth, z (as illustrated in Fig. 7). Using $x = a_0 + a_1 z$ as an example, we compute the sum of the squared predicted errors, SS_{error}:

$$SS_{error} = \sum_{i=1}^{n} (x_i - \hat{x}_i)^2 = \sum_{i=1}^{n} (x_i - \hat{a}_0 - \hat{a}_1 z_i)^2$$

(1)

Here, $\hat{a}_0$ and $\hat{a}_1$ are unbiased estimators for a_0 and a_1. We then estimate the standard error for $\hat{a}_1$, $SE(\hat{a}_1)$, as:

$$SE(\hat{a}_1) = \frac{SS_{error}/(n-1)}{\sqrt{(n-1)S_z^2}}$$

(2)

Here n is the number of data points in the fit and S_z^2 is the variance of z. Then, the 90% confidence interval for the slope is $\hat{a}_1 \pm SE(\hat{a}_1)t_{0.05,n-2}$, where the value of $t_{0.05,n-2}$ taken from standard t-distribution tables [25]. An analogous procedure was applied to $y = b_0 + b_1 z$ to obtain 90% confidence intervals for $\hat{b}_1$. Since only the direction of the fitted lines is of interest in our analysis, we do not compute confidence intervals for $\hat{a}_0$ or $\hat{b}_0$. Finally, to convert our uncertainty estimates for $\hat{a}_1$ and $\hat{b}_1$ to the angular deviations listed in Table I, we enumerated the four extremal combinations of centerline orientations

16

$$([\hat{a}_1 + SE(\hat{a}_1)t_{0.05,n-2}, \hat{b}_1 + SE(\hat{b}_1)t_{0.05,n-2}], [\hat{a}_1 + SE(\hat{a}_1)t_{0.05,n-2}, \hat{b}_1 - SE(\hat{b}_1)t_{0.05,n-2}],$$

$$[\hat{a}_1 - SE(\hat{a}_1)t_{0.05,n-2}, \hat{b}_1 + SE(\hat{b}_1)t_{0.05,n-2}], [\hat{a}_1 - SE(\hat{a}_1)t_{0.05,n-2}, \hat{b}_1 - SE(\hat{b}_1)t_{0.05,n-2}]) \text{ and}$$

used the one with the largest deviation angle as our angular uncertainty estimate.

For CTB planes, the uncertainty of a deviation angle is taken to be the difference between the largest deviation angle obtained from these extremes and the best-fit deviation angle. For <110>-type directions, the uncertainty is taken to be the deviation angle of these extremes to the best-fit centerline. This analysis allows us to conclude that all the cavities lie within their corresponding CTB planes, to within the computed uncertainty.

Of the eleven cavities reported in TABLE I, five are aligned with <110>-type directions to within the computed uncertainty while four others lie only marginally beyond that range. A single cavity (site H) appears to be aligned with a different crystallographic direction within the CTB plane, namely a <123>-type direction. However, only four pairs of centerline coordinates were fitted for this cavity, resulting in a markedly elevated orientation uncertainty. Finally, the centerline of one cavity (site B) appears to vary with depth beneath the surface. The tortuosity of this centerline may be due to the cavity growing along different <110>-type directions at different depths. Alternatively, it may be caused by the cavity reaching a triple junction beneath the sample surface and growing along a different grain boundary than the CTB on which it initiated.

The foregoing analysis shows that cavities are preferentially aligned along <110>-type directions within CTB planes, as illustrated in FIG. 8. This result is consistent with the observed "fin", "palm leaf", and "arrow head" morphologies reported in the trench morphology section, as all may be formed by cavities lying along <110> type directions. In the "fin" morphology, all

cavities are aligned with one single <110>-type direction (e.g., E and F, I and J in FIG. 5). "Palm leaf" and "arrow head" morphologies involve cavities along two different <110>-type directions within a single CTB plane. The angles between these cavities is ~60° (e.g., C and D for palm leaf, M and N for arrow head in FIG. 5).

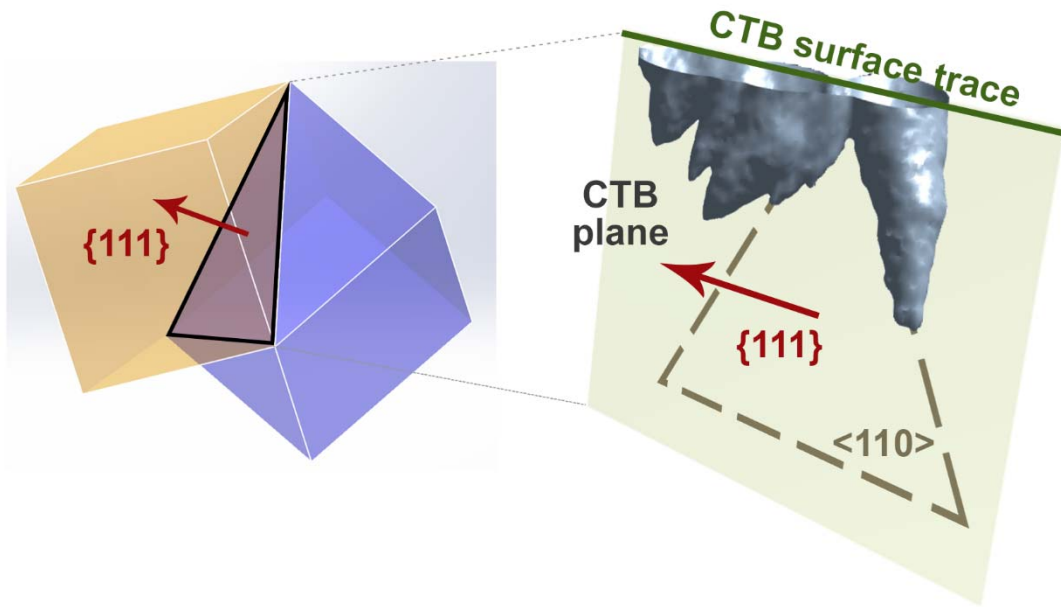FIG. 8. Cavities are preferentially aligned with <110>-type directions within CTB planes. The cavities displayed in this figure are from site 1, shown in FIG. 2.a)

D. Corrosion trenches on non-CTBs

In addition to numerous corrosion trenches on CTBs, we also found corrosion trenches on three non-CTBs. Of these three non-CTBs, one was inadvertently destroyed when the sample was sectioned to confirm lack of sub-surface oxide films (see section III.B). Performing EBSD

analysis on the remaining two non-CTBs, we found that one is a Σ11 GB and the other is a Σ39b. We analyzed the orientation of the corrosion trenches on these two remaining non-CTBs based on our CT data. We then computed the best-fit normal vectors to these trenches following the same procedure as described in the preceding subsection.

Our analysis of corroded CTBs revealed that trenches along these boundaries lie along the CTB plane. Assuming that the trenches on the corroded non-CTBs also lie along GB planes, the normal vector to these trenches provides us with the additional information needed to describe the complete crystallographic character of both of these boundaries. We used this information to construct atomic-scale models of both corroded non-CTB GBs and to compute their boundary energies.

We constructed our GB models in 15 nm × 15 nm × 15 nm simulation cells containing ~0.3M atoms. The models are bicrystals containing two grains, each rotated into the crystallographic orientation determined by EBSD measurements on our sample. Each grain is sectioned along the plane with normal direction determined from the above-mentioned analysis of corrosion trenches. When the two grains are joined, we obtain GB models with identical crystallographic character to that found in our experiments. The models terminate with free surfaces on all sides. Fig. 9 shows a cross section through the model for the Σ39b GB, indicating the location of grains, GB, and free surfaces.

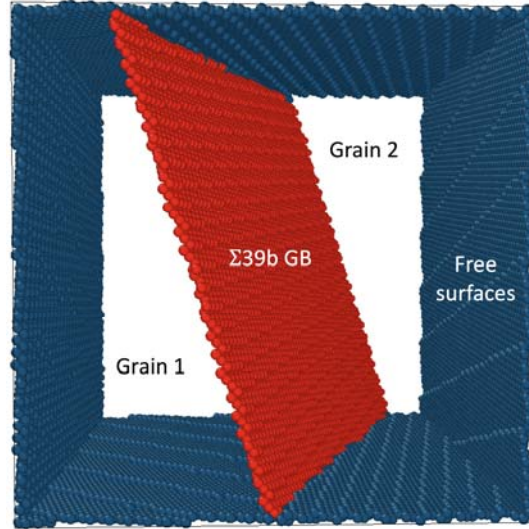Fig. 9: Cross section through a fully-relaxed, atomic-scale model for the corroded Σ39b GB found in our sample. For clarity, atoms with perfect FCC local structure are not shown.

These models were relaxed using conjugate gradient energy minimization using the EAM potential for Ni by Zhou *et al.* [26]. To compute the energy of the GBs, we followed a procedure similar to that used by Vattré *et al.* [27]. First, we summed up the atomic energies of all N atoms that are within 13nm of the GB plane and no closer than 1nm to a free surface. This way, we exclude the effect of free surfaces on our energy calculation. We then subtract from this sum an energy equal to the product of the cohesive energy per atom and the number of atoms, N. This calculation yields the Gibbsian excess energy over the GB area, A, contained within the aforementioned set of N atoms. Diving this excess energy by A, we obtain the GB energy. Our calculation revealed that the corroded Σ11 has an energy of ~1.3 J/m^2 and the corroded Σ39b has an energy of ~1.4 J/m^2. Comparing these energies to the GB energy distribution reported in Refs.[28-30], we conclude that both boundaries are among the highest energy boundaries that may be expected in polycrystalline Ni.

IV. DISCUSSION

Our work demonstrates the occurrence of intergranular corrosion in pure Ni during cathodic charging. This observation contrasts with previous reports of intergranular corrosion taking place mostly on anodic surfaces [1]. Moreover, contrary to suggestions that CTBs are corrosion resistant [6], we show that, in Ni, they are especially susceptible to corrosion under extreme cathodic polarization.

Our finding is surprising in light of the extremely low grain boundary energy of CTBs in Ni [1,30]: a fact that motivates the initial expectation of corrosion resistance in these boundaries. However, the preferential orientation of corrosion cavities along <110>-type directions within CTB planes sheds light on potential mechanisms underlying the unexpected corrosion susceptibility of CTBs. Most GBs that appear to be perfect CTBs in EBSD scans actually have planes offset by a few degrees from a perfect {111} orientation [31,32]. Both experimental [33] and modeling [34] studies indicate that this deviation is accommodated by occasional SITB facets of nanometer-scale width.

SITBs have the same Σ3 misorientations as CTBs. However, their GB planes are aligned with {112}-type planes in the adjacent crystals, rather than {111} planes. Thus, SITB facets intersect CTB facets at right angles and the line of intersection between them lies along a <110>-type direction. Consequently, the preferential <110> orientation of corrosion cavities is consistent with their initiation on and subsequent growth along SITB facets. Any given near-CTB boundary may initiate numerous such cavities, which coalesce with their neighbors as they grow, eventually giving rise to trenches along CTBs. Thus, even though preferential intergranular

corrosion may actually initiate along SITBs rather than CTBs, the ensuing corrosion process generates extended, linear notches that are in fact aligned with CTBs. Direct observation of cavity initiation at SITBs is a valuable objective for future studies.

The energy of SITBs in Ni is ~0.8 J/m^2, i.e., considerably higher than the energy of CTBs—0.3 J/m^2—yet also much lower than that of the highest energy GBs in Ni, which are in the 1.2-1.4 J/m^2 range [28,30]. Thus, it is to be expected that SITBs are more susceptible to corrosion than CTBs. However, based on energy alone, it is not clear why our sample did not present more cases of corrosion on general, high energy GBs. One potential explanation is that such boundaries are not frequently encountered in the GB network of polycrystalline Ni. Indeed, measurements of full GB crystallographic character distributions in polycrystalline Ni show that the proportion of GBs of given character in a microstructure is inversely correlated to their energy [29]. Thus, since they have the lowest energy of any GBs in Ni, CTBs are by far the most frequently encountered GBs in this metal. Consequently, since most of them contain SITB facets, it may be expected that the majority of corrosion cavities are found on CTBs.

However, we did also observe three instances—i.e., ~3.3% of the total number—of corrosion cavities occurring on non-CTBs. As described in section III.D, we were able to compute the energies of two of these boundaries under the assumption that the corrosion trenches that form on them lie along the GB planes. We found that these boundaries have relatively high energies of ~1.3 J/m^2 and ~1.4 J/m^2. Moreover, the data presented by Li *et al* [29] allow us estimate that approximately ~5.7% of all GBs in the polycrystalline Ni samples they investigated have energies higher than that of a SITB. This fraction compares well with the fraction of corroded non-CTBs in our sample. Of course, the true GB character distribution in any material depends on processing history and is likely to differ in our sample from that in the sample analyzed by Li

et al [29]. In particular, given the extended, high-temperature annealing we used in our investigation, it is probable that the fraction of high energy boundaries in our samples is low. Thus, it appears plausible that the three corroded non-CTBs were the only GBs in our sample with energies higher than a SITB. The foregoing consideration militate in favor of the conclusion the corrosion susceptibility of GBs in Ni is ultimately determined primarily by GB energy.

Based on previous research [22,35-38], we hypothesize that the formation of corrosion cavities consists of two distinct stages. The first is breakdown of the surface oxide. Pure Ni has good corrosion resistance because of its stable oxide layer (passive layer) [39]. However, even when protected by passive layers, metal surfaces are nevertheless susceptible to localized corrosion: passive layers may break down at isolated sites while the remainder of the film continues to protect the surface from general corrosion [40]. The passive layer on pure Ni consists of a hydroxide outer layer and a NiO inner layer [22]. In acid solution, the dissolution of the passive layer follows the reaction $NiO + 2H^+ + 2e \rightarrow Ni + H_2O$ [38]. This reaction is expected to occur faster around defects, such as GB surface traces, leading to the preferential initiation of localized corrosion there. The details of passive film breakdown near microstructural defects is not well understood and may well be sensitive to trace levels of impurities, such as individual segregated atoms or nano-scale clusters. Since such impurities are below the detection limits of the characterization methods used in the present study, further investigation of the initial stages of passive film breakdown would require transmission electron microscopy, atomic probe tomography, or other high-resolution/low volume methods.

The second stage of the corrosion process is the formation of a local galvanic cell between the bottom of the cavity and the sample surface. Classical electrostatics predicts that a non-uniform surface topography gives rise to location-dependent differences in surface potential. Using

numerical and experimental methods, Cheng *et al.* showed that, under cathodic polarization, the potential at the bottom of a cavity is anodic relative to the surrounding flat surface [35,36]. Thus, the bottom of a cavity, such as those observed in our study, actually constitutes the anode of a miniature, local galvanic cell while the remainder of the Ni surface acts as the cathode. This potential difference drives a near-surface current, allowing the Ni at the bottom of the cavity to continuously dissolve, deepening the cavity and further increasing the potential difference [37].

It bears emphasizing that, in the cavity formation process proposed above, the main role of SITBs is only to initiate the corrosion cavities. Once initiated, these cavities are expected to grow in an autocatalytic manner because the potential difference from the sample surface to the bottom of a corrosion cavity forms a local galvanic cell, driving material removal from the cavity interior. Thus, once initiated, a cavity may grow regardless of the energy of the surrounding material. Indeed, in the sample analyzed here, such cavities grow not only into low energy CTB facets, but also into the surrounding perfect crystal, which has lower energy than any grain boundary. As a cavity grows, it eventually overlaps with neighboring cavities. If many cavities are pre-aligned along a single grain boundary—e.g., along CTBs, as is the case in our sample— they may coalesce into long, linear trenches.

The mechanism proposed above contrasts with putative explanations for degradation of CTBs under mechanical loading. Several researchers have observed that CTBs in FCC metals are preferential crack initiation sites under fatigue loading [41,42]. Seita *et al.* showed that CTBs also preferentially initiate cracks in hydrogen-embrittled Ni-base alloy 725 [43]. In both of these examples, degradation appears to be tied to slip along the CTB plane [20,44], whereas the samples investigated in the present study were not subject to any deformation. Thus, the mode of CTB degradation reported here is fundamentally distinct from those reported previously for

mechanically loaded Ni. Determining whether there are any synergistic or competitive effects between these modes is an intriguing topic for future research.

Our findings have important consequences for the technological use of Ni and Ni-base alloys. In aqueous media, localized corrosion typically occurs on anodically polarized surfaces [45] while cathodically polarized surfaces are expected to exhibit no or minimal alteration [46]. Our work shows that extreme cathodic polarization may nevertheless give rise to localized corrosion. Similar, pit-like features have also been observed on cathodically protected carbon steel [35] and Al-Mg alloy [47]. These results show that cathodic protection cannot be expected to prevent corrosion under the most extreme conditions, motivating further studies to determine the limits of cathodic protection.

Another technological consequence of our work is that maximizing the fraction of CTBs in a microstructure may not be the ideal goal of GB engineering approaches to improving corrosion resistance. Indeed, if GB energy determines susceptibility to intergranular corrosion, then the type of GB to be favored by GB engineering is one that minimizes the energy of the highest energy facet that may be formed by perturbing the GB plane. This criterion calls for further exploration of the GB character space in Ni in search of corrosion resistant boundaries. If CTBs do not meet this criterion (on account of the relatively high energy of SITBs), then GB engineering should aim to reduce, rather than maximize, the fraction of CTBs in the microstructure.

Finally, the identification of CTBs as the sites most susceptible to corrosion under extreme cathodic charging leads to opportunities for improved lifetime predictions for components made of Ni or Ni-based alloys. Robust and inexpensive optical methods of characterizing surface microstructure may make it possible to routinely determine the fraction and alignment of CTBs

25

in finished products [48]. Based on this information, users may decide to prevent especially susceptible components from entering service or delay withdrawal from service of components that are least susceptible.

ACKNOWLEDGEMENTS

References

[1]   G. Palumbo and K. Aust, Acta Metall. Mater. **38**, 2343 (1990).
[2]   G. Palumbo and K. Aust, ScM **22**, 847 (1988).
[3]   G. Palumbo and K. Aust, Mater. Sci. Eng. A **113**, 139 (1989).
[4]   Y. Li and Y. F. Cheng, Appl. Surf. Sci. **366**, 95 (2016).
[5]   S. H. Kim, U. Erb, K. T. Aust, and G. Palumbo, Scripta Mater. **44**, 835 (2001).
[6]   V. Randle, Acta Mater. **52**, 4067 (2004).
[7]   G. Palumbo, P. J. King, K. T. Aust, U. Erb, and P. C. Lichtenberger, ScMM **25**, 1775 (1991).
[8]   S. Xia, H. Li, T. G. Liu, and B. X. Zhou, J. Nucl. Mater. **416**, 303 (2011).
[9]   C. Hu, S. Xia, H. Li, T. Liu, B. Zhou, W. Chen, and N. Wang, Corros. Sci. **53**, 1880 (2011).
[10]   P. Jakupi, J. J. Noël, and D. W. Shoesmith, Electrochem. Solid-State Lett. **13**, C1 (2010).
[11]   I. Roy, H. W. Yang, L. Dinh, I. Lund, J. C. Earthman, and F. A. Mohamed, Scripta Mater. **59**, 305 (2008).
[12]   E. Martinez-Lombardia, L. Lapeire, V. Maurice, I. De Graeve, K. Verbeken, L. H. Klein, L. A. I. Kestens, P. Marcus, and H. Terryn, Electrochem. Commun. **41**, 1 (2014).
[13]   A. Turnbull, Proc. R. Soc. A **470**, 20140254 (2014).
[14]   M. Ghahari, D. Krouse, N. Laycock, T. Rayment, C. Padovani, M. Stampanoni, F. Marone, R. Mokso, and A. J. Davenport, Corros. Sci. **100**, 23 (2015).
[15]   F. A. Almuaili, S. A. McDonald, P. J. Withers, A. B. Cook, and D. L. Engelberg, Corros. Sci. **125**, 12 (2017).
[16]   L. T. Popoola, A. S. Grema, G. K. Latinwo, B. Gutti, and A. S. Balogun, Int. J. Ind. Chem. **4**, 35 (2013).
[17]   Y.-c. K. Chen-Wiegart *et al.*, in *AIP Conf. Proc.* (AIP Publishing, 2016), p. 030004.
[18]   L. Li, H. Yan, W. Xu, D. Yu, A. Heroux, W.-K. Lee, S. I. Campbell, and Y. S. Chu, in *SPIE Optical Engineering + Applications* (SPIE, 2017), p. 8.
[19]   J. A. Leavitt, L. C. McIntyre, M. D. Ashbaugh, J. G. Oder, Z. Lin, and B. Dezfouly-Arjomandy, Nucl. Instrum. Methods Phys. Res., Sect. B **44**, 260 (1990).
[20]   M. Seita, J. P. Hanson, S. Gradečak, and M. J. Demkowicz, J. Mater. Sci. **52**, 2763 (2017).
[21]   S. Perusin, D. Monceau, and E. Andrieu, J. Electrochem. Soc. **152**, E390 (2005).
[22]   D. Zuili, V. Maurice, and P. Marcus, J. Electrochem. Soc. **147**, 1393 (2000).
[23]   U. Krupp, P. E. G. Wagenhuber, W. M. Kane, and C. J. McMahon, Mater. Sci. Technol. **21**, 1247 (2005).
[24]   S. Yamaura, Y. Igarashi, S. Tsurekawa, and T. Watanabe, Acta Mater. **47**, 1163 (1999).
[25]   D. C. Montgomery and G. C. Runger, *Applied statistics and probability for engineers* (John Wiley and Sons, 2014).
[26]   X. Zhou, R. Johnson, and H. Wadley, PhRvB **69**, 144113 (2004).
[27]   A. Vattré, N. Abdolrahim, S. S. Navale, and M. J. Demkowicz, Extreme Mechanics Letters **28**, 50 (2019).
[28]   A. Hallil, A. Metsue, J. Bouhattate, and X. Feaugas, Philos. Mag. **96**, 2088 (2016).
[29]   J. Li, S. J. Dillon, and G. S. Rohrer, Acta Mater. **57**, 4304 (2009).
[30]   D. L. Olmsted, S. M. Foiles, and E. A. Holm, Acta Mater. **57**, 3694 (2009).
[31]   V. Randle, J. Mater. Sci. **30**, 3983 (1995).
[32]   V. Randle, M. Caul, and J. Fiedler, Microsc. Microanal. **3**, 224 (1997).
[33]   J. Wang, O. Anderoglu, J. Hirth, A. Misra, and X. Zhang, Appl. Phys. Lett. **95**, 021908 (2009).
[34]   J. Wang, N. Li, and A. Misra, Philos. Mag. **93**, 315 (2013).
[35]   Z. Liu, X. Li, and Y. Cheng, Electrochim. Acta **60**, 259 (2012).

[36]   L. Xu and Y. Cheng, Corros. Sci. **78**, 162 (2014).
[37]   S. Y. Li, Y. G. Kim, Y. T. Kho, and T. Kang, CORROSION **60**, 1058 (2004).
[38]   B. MacDougall and M. Cohen, J. Electrochem. Soc. **123**, 191 (1976).
[39]   V. Maurice, H. Talah, and P. Marcus, Surf. Sci. **304**, 98 (1994).
[40]   E. McCafferty, *Introduction to corrosion science* (Springer, New York, NY, 2010).
[41]   W. Abuzaid, A. Oral, H. Sehitoglu, J. Lambros, and H. J. Maier, Fatigue Fract. Eng. Mater. Struct. **36**, 809 (2013).
[42]   M. D. Sangid, H. J. Maier, and H. Sehitoglu, Int. J. Plast. **27**, 801 (2011).
[43]   M. Seita, J. P. Hanson, S. Gradečak, and M. J. Demkowicz, Nat. Commun. **6**, 6164 (2015).
[44]   L. L. Li, Z. J. Zhang, P. Zhang, Z. G. Wang, and Z. F. Zhang, Nat. Commun. **5**, 3536 (2014).
[45]   H. Kaesche, *Metallic corrosion* (NACE, 1985).
[46]   P. Pedeferri, Constr. Build. Mater. **10**, 391 (1996).
[47]   K. Jafarzadeh, T. Shahrabi, and M. Hosseini, Corros. Eng, Sci. Technol. **44**, 144 (2009).
[48]   M. Seita, M. M. Nimerfroh, and M. J. Demkowicz, Acta Mater. **123**, 70 (2017).